Supporting Information for "Bright, mechanosensitive upconversion with cubic-phase heteroepitaxial core-shell nanoparticles"

Alice Lay,[*,†] Chris Siefe,[‡] Stefan Fischer,[‡] Randy D. Mehlenbacher,[‡] Feng Ke,[¶] Wendy L. Mao,[¶] A. Paul Alivisatos,[§,‖,⊥,#] Miriam B. Goodman,[@] and Jennifer A. Dionne[*,‡]

†*Department of Applied Physics, Stanford University, Stanford, CA 94305*

‡*Department of Materials Science and Engineering, Stanford University, Stanford, CA 94305*

¶*Department of Geological Sciences, Stanford University, Stanford, CA 94305*

§*Department of Chemistry, University of California, Berkeley, CA 94720*

‖*Department of Materials Science and Engineering, University of California, Berkeley, CA 94720*

⊥*Materials Sciences Division, Lawrence Berkeley National Laboratory, Berkeley, CA 94720*

#*Kavli Energy NanoScience Institute, Berkeley, CA 94720*

@*Department of Molecular and Cellular Physiology, Stanford University, Stanford, CA 94305*

E-mail: alay@stanford.edu; jdionne@stanford.edu

Contents

1 Methods

1.1 Synthesis of cores and core-shell nanoparticles

To synthesize cubic-phase core-shell nanoparticles, we modified a procedure detailed by Li et al.[1] Reagents include Gadolinium oxide (Gd_2O_3), Lutetium oxide (Lu_2O_3), 99% trifluoroacetic acid (TFA), Sodium trifluoroacetate ($NaCF_3CO_2$), 90% 1-octadecene (ODE), 70% oleylamine (OM), and 90% oleic acid (OA) from Sigma-Aldrich. Yttrium trifluoroacetate ($Y(CF_3COO)_3$), Ytterbium trifluoroacetate ($Yb(CF_3COO)_3$), and Erbium trifluoracetate ($Er(CF_3COO)_3$) were purchased from GFS Chemical. All chemicals were used as received.

Large batch synthesis of $NaYF_4$:Yb,Er cores. In a 250 mL round bottom flask, we mixed 16 mL OA, 32 mL ODE, 5 mmol $Na(CF_3COO)$ (5 mL of 1 M stock solution in DI water), and 5 mmol $Ln(CF_3COO)_3$ with Ln = 80% Y, 18% Yb, and 2% Er (total 25 mL of 0.2 M stock solutions in DI water). The mixture was heated to 150°C for 1 hour to boil off water and then cooled to 50°C before adding 16 mL OM. Upon adding OM, we increased the stirring rate to ~1200 rpm and temperature to 100°C. We let the mixture stir under vacuum for 30 min at 100°C, purged it with argon gas, and then heated it to 310°C. After 20 minutes, the heating mantle is removed and the sample is allowed to cool to room temperature under constant stirring. Smaller cores were achieved by reducing the Na^+ and Ln^{3+} concentration by half (0.5 mmol each), or equivalently increasing the OD and OA concentration by 2x. Meanwhile, larger cores were achieve by increasing the OD:OA concentration ratio from 2 to 4.7.

Cleaning procedure. Solution from the flask was collected with ethanol into centrifuge tubes and spun at 3000 RCF or G-Force for 10 min. We poured out the supernatant and resuspended the pellet in ethanol for another wash (3000 RCF for 5 min). For the third and final wash (3000 RCF for 5 min), the pellet was suspended in 2-3 mL cyclohexane and 20 mL ethanol. Nanoparticles were stored in 25 mL cyclohexane before they were shelled or characterized.

Preparation of $Gd(CF_3COO)_3$ as shell precursor. In a round bottom flask, 5 mmol Gd_2O_3 was mixed with 5 mL TFA and 5 mL DI water at 80°C, until the solution turned clear. The temperature was then increased to 100°C to slowly evaporate the solvent, leaving a residual white powder. Thereafter, the flask was placed in a vacuum chamber to fully dry. The product was dissolved in 50 mL DI water to achieve a 0.2 M stock solution.

Preparation of $Lu(CF_3COO)_3$ as shell precursor. Following a procedure reported by Fischer et al.,[2] 1 mmol Lu_2O_3 was dissolved in 3 mL TFA and 20 mL DI water at 90°C. The flask was capped to prevent evaporation during the ∼8 hours it took for the solution to turn clear. Afterwards, the flask was uncapped and the temperature lowered to 65°C for evaporation overnight. Again, this left a residual white powder, which was fully dried and dissolved in 10 mL DI water for a 0.2 M stock solution.

Shelling $NaYF_4$:Yb,Er cores. In a 50 mL flask, we added 5 mL OA, 5 mL ODE, 0.2 mmol $Na(CF_3COO)$ (0.2 mL of 1 M stock solution), and 0.2 mmol $Ln(CF_3COO)_3$ where Ln = Gd, Lu, or Y (1 mL of 0.2 M stock solution). The mixture was heated to 150°C for 1 hour to remove solvents and cooled to 50°C before adding 1 mL $NaYF_4$:Yb,Er cores. We increased the stirring rate, heated the mixture to 100°C, and pulled it under vacuum for 30 min. After an argon purge, the mixture was heated to 310°C and allowed to react at that temperature for 30 min. Finally, we let the solution cool to room temperature and clean the nanoparticles as mentioned above.

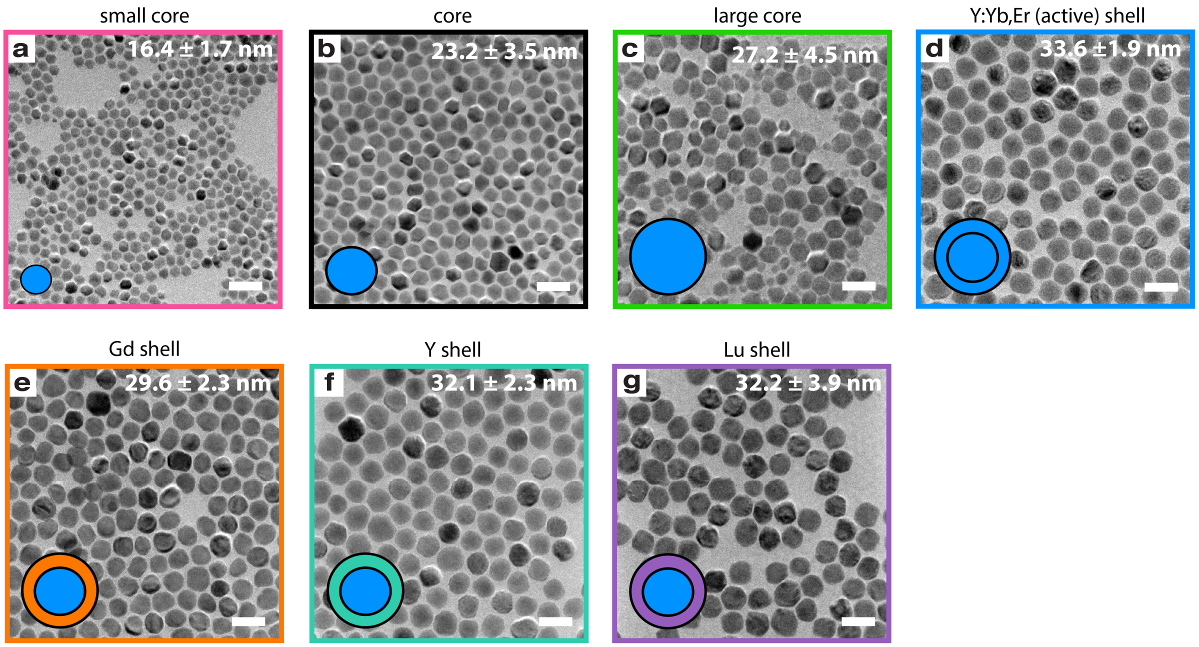

Figure S1: Transmission electron micrographs of all core and core-shell nanoparticles a-c) The size series includes cores that are smaller and larger than the ones used in our main study (b). As a control for both size and the shelling procedure, we shell the core with an active, Y:Yb,Er, material (d). e-g) Cores with inert shells. The scale bar is 50 nm.

1.2 Particle analysis

To determine the size distribution of our nanoparticles, we take transmission electron micrographs (TEMs) containing ∼100 to 300 nanoparticles (Figure S1). We then process the images using ImageJ software by setting a threshold pixel value to maximize the contrast between the nanoparticles and the background before running particle analysis. For cores, which have a hexagonal 2D projection (Figure S3a), we measure the area (A_c) of each nanoparticle and determine the diameter (d_c) as the long diagonal from vertex to vertex or $d_c = \sqrt{\frac{8 \cdot A_c}{3\sqrt{3}}}$. In contrast, core-shell nanoparticles have a spherical morphology (Figure S3b). As a result, the diameter (d_s) is calculated from the measured area (A_s) as $d_s = 2\sqrt{\frac{A_s}{\pi}}$. In Figure S2, we display histograms of the diameter values for all of our nanoparticle samples. Additionally, histograms are fitted to a probability density function, highlighting the mean size and standard deviation.

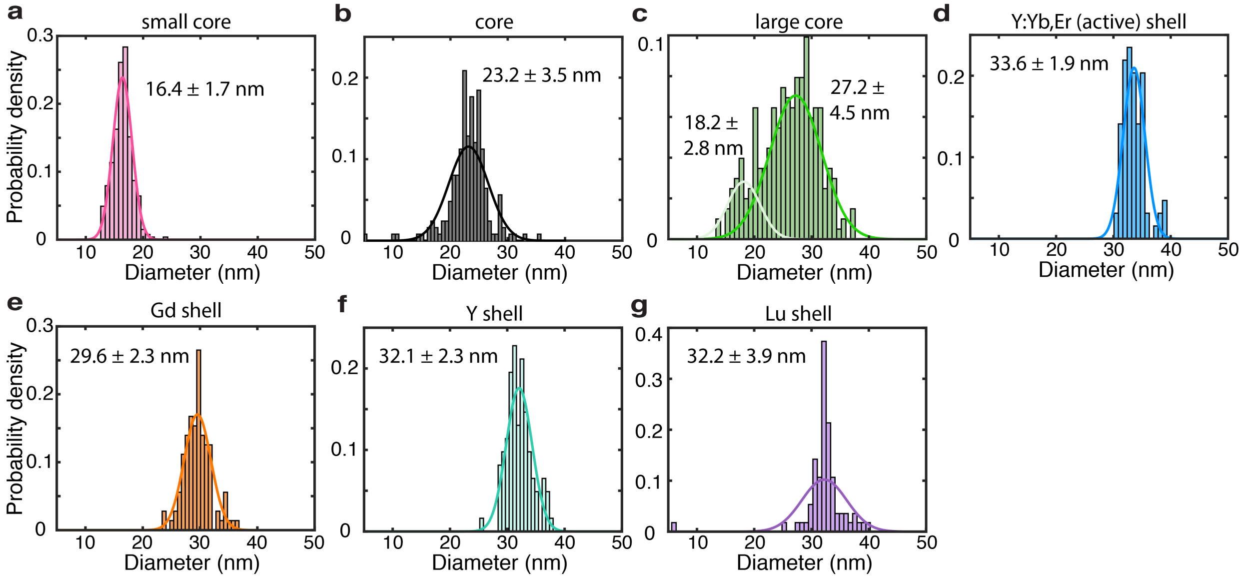

Figure S2: Size distribution of nanoparticles
Histograms showing size distribution of ∼100-300 nanoparticles each. Cores have a hexagonal morphology, so diameters are defined as the long diagonal from vertex to vertex, while diameters for core-shell nanoparticles are derived from their spherical morphology. For each histogram, a Gaussian probability density function curve is fitted to extract the mean size and standard deviation of the UCNPs. The large core sample has a bimodal size distribution, indicating limitations in the synthesis to achieve larger cubic-phase core sizes.

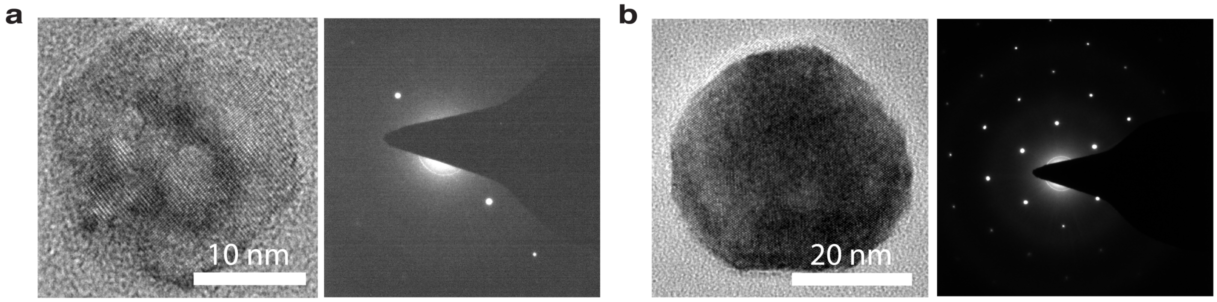

Figure S3: Single particle diffraction pattern
α-NaYF$_4$ has a zinc blende crystal structure. Diffraction images show the crystalline nature of the a) hexagonal-shaped core and b) spherical core-shell structure. In b) the diffraction pattern has a zone axis of $[1\bar{1}1]$.

1.3 Structural characterization with X-ray diffraction

Thin films are prepared by dropcasting nanoparticles on a glass slide. We collect X-ray diffraction (XRD) data with a Cu Kα_1 X-ray source (λ = 1.54056 Å) on an X'Pert X-ray diffractometer (PANalytical B.V.). Diffraction peaks are matched to references from the International Centre for Diffraction Data (ICDD), confirming pure cubic-phase samples and showing differences from core to core-shell nanostructures. To determine lattice constants, we process the peaks through a least-squares Pawley[3] fit on PANalytical HighScore Plus software. We constrain the crystal class to Fm-$\bar{3}$m, account for asymmetry in the peak shape, and perform the fitting procedure 10 times for convergence, such that residuals or R-values are < 2.5%. We round lattice constants to a hundredth of an Angstrom. Figure S4 shows the diffraction patterns for the core size series. In contrast to the core-shell series (Figure 2), there is no significant strain or change in the lattice parameter.

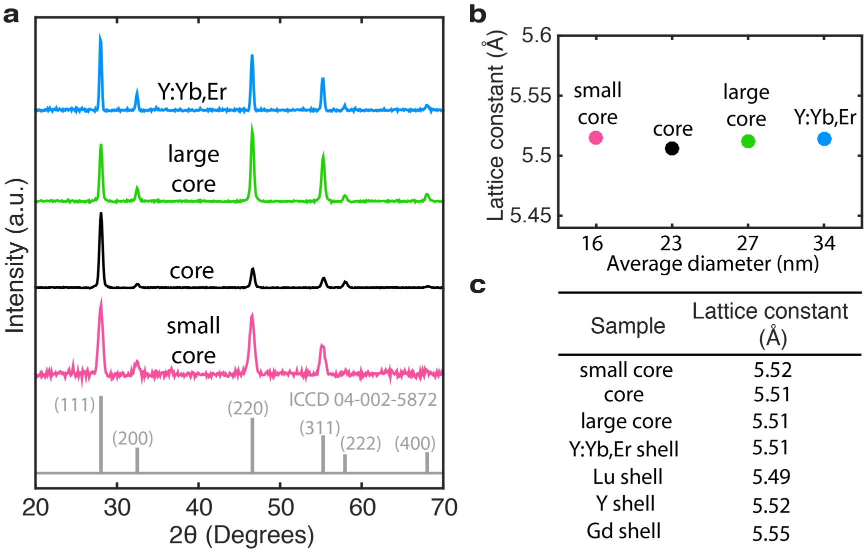

Sample	Lattice constant (Å)
small core	5.52
core	5.51
large core	5.51
Y:Yb,Er shell	5.51
Lu shell	5.49
Y shell	5.52
Gd shell	5.55

Figure S4: Structural characterization for size series
a) XRD patterns acquired using Cu Kα_1 X-rays (λ = 1.54056 Å) for cores of various sizes and the active core-shell control. The active core-shell matches ICDD standard pattern 04-002-5872. For cores, the relative peak intensities change with size, perhaps most pronounced between (111) and (220). This change in relative lattice parameter indicates modifications in stoichiometry or geometry through synthesis. As expected, there are no significant lattice parameter shifts in b), compared to Lu- and Gd-shelled structures listed in c).

1.4 Quantum yield measurements and calculations

Optical setup. Upconversion quantum yield (UCQY) measurements are obtained using the custom experimental setup illustrated in Figure S5. For reference, this is the same experimental setup used and described previously.[2,4] For our near infrared source, we use a MDL-III-980 2-Watt continuous-wave laser from Changchun New Industries emitting at 977.5 nm with a full-width at half maximum of 3 nm and a power stability of 0.185% over a four-hour period. This laser is fiber coupled through a 400 µm optical fiber and re-collimated to improve the beam profile. A lens is used to focus the laser beam onto the sample position. Illumination power density is determined by picking off a fraction of the beam and sending it to an S401C power meter from Thorlabs, Inc. This pick-off continuously measures the laser power and corrects for fluctuations in laser power over the course of experiments.

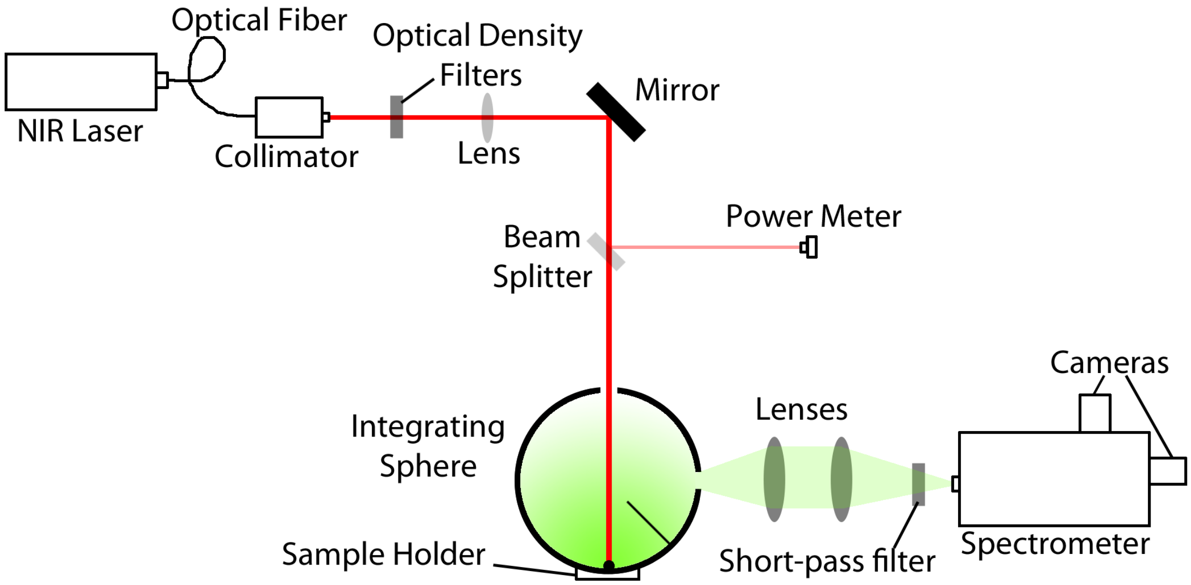

Figure S5: Experimental setup for quantum yield measurements

The laser enters a 5.3-inch inner diameter Labsphere integrating sphere coated with Spectralon where it illuminates the sample. Diffuse light, including light emitted from the sample, exits the integrating sphere at a port orthogonal to the laser entry port. A baffle prevents direct reflections from being detected. Upon exiting the integrating sphere, the emitted signal from the sample passes through two lenses, guiding and magnifying the collected light, and an 850 nm short-pass filter from Edmund Optics, Inc. The short-pass filter functions to attenuate the 980 nm laser beam, but has 50% transmission for wavelengths above 1350 nm. The light then reaches a Princeton Instruments SP2300 spectrometer and is diffracted using a 300 groove/mm grating and imaged using a Princeton Instruments PIXIS 400B silicon CCD-camera or Andor InGaAs camera.

Calibration and beam profile. This system is calibrated using a NIST-traceable radiometric calibration source (OceanOptics, HL-CAL-3plus, Serial Number 089440003, Calibration Number 19936) which was placed in the entry port of the integrating sphere and directed at the sample position. This source was used to measure the spectral sensitivity function of the system across the complete Erbium emission spectrum. The beam profile is measured at the beginning of the experiment using a beam profiler (DataRay, WinCamD-UCD12-1310). The beam area is calculated by counting the pixels for which 72% (one sigma for 2D Gaussian profile) of the total photon flux from the laser is reached. We achieve a beam area of 0.0075 ± 0.0009 cm^2.

Sample loading and spectra collection. Approximately 1.5 mL of each sample, UCNPs suspended in cyclohexane, is prepared and transferred to a quartz cuvette. In addition, we prepare a reference sample with only the solvent, cyclohexane. The cuvette is inserted into the integrating sphere, opposite the beam entry port. We collect spectra at the Si-CCD camera with the grating centered at 600 nm and then 900 nm. We also take spectra using the InGaAs camera with the grating centered at 1500 nm. For each sample, this collection procedure is repeated four times.

QY calculation. Using the sample and reference spectra, the number of photons (in the visible and in the infrared) emitted by and the number of NIR photons absorbed by the sample can be determined. Here we define upconversion quantum yield as the number of visible photons emitted by the sample divided by the number of NIR photons absorbed by the sample. This calculation is as follows:

$$UCQY = \frac{\int f_{cor,em}(\lambda)/T_{filter}(\lambda)(S_{sample,em}(\lambda) - c_{blank,em}S_{blank,em}(\lambda))d\lambda}{\int f_{cor,abs}(\lambda)/T_{filter}(\lambda)(c_{sample,abs}S_{sample,abs}(\lambda) - c_{blank,abs}S_{blank,abs}(\lambda))d\lambda} \tag{1}$$

where $f_{cor,em}$ and $f_{cor,abs}$ are the spectral sensitivity of the setup for the given grating center wavelength, T_{filter} is the transmittance of the 850 nm short-pass filter, $S_{sample,em}$ is the sample emission spectrum centered at 600 nm, $S_{sample,abs}$ is the laser spectrum with the sample in the integrating sphere centered at 900 nm, $S_{blank,em}$ is the blank emission spectrum centered at 600 nm, $S_{blank,abs}$ is the laser spectrum with the blank inside the integrating sphere at a center wavelength of 900 nm, and the parameters c_{xy}, where $x = sample, blank$ and $y = em, abs$, are power correction factors for laser intensity fluctuations. The parameters c_{xy} are calculated as follows:

$$c_{xy} = \frac{P_{xy}}{P_{sample,emission}} \tag{2}$$

These parameters are normalized to the power measurement of the sample emission, because upconversion is a non-linear process. These values are ~1 due to the good power stability of the laser.

These UCQY values can be separated into the green and red UCQY. The green UCQY is calculated by integrating the green regions of the Er^{3+} spectrum and dividing by the number of absorbed NIR photons, and similarly the red with the red regions of the Er^{3+} spectrum. The total UCQY is then simply the sum of the individual red and green contributions. For each sample, the UCQY is calculated from acquired spectra. The error is propagated from both the statistical and systematic error of the measurement.

1.5 Lifetime measurements

Excited-state lifetimes are measured for both upconversion and direct excitation. Upconversion excitation refers to exciting nanoparticles with 980 nm light and monitoring emission from the Er^{3+} states: $^2H_{11/2}$, $^4S_{3/2}$, and $^4F_{9/2}$. These states are populated via energy transfer upconversion, and thus, measuring the lifetime of these states when excited by upconversion provides insight to the upconversion pathway. In contrast, direct excitation refers to directly exciting the states of interest to remove the convolution of the lifetimes with upconversion processes. The methods used for obtaining lifetime measurements have been previously reported.[2,4]

All lifetime measurements are performed using an Edinburgh Instruments FLS980 spectrometer. Emission is monitored using one of two Hamamatsu photomultiplier tubes (PMT). A TE-An Opotek HE 355 LD optical parametric oscillator (OPO) tunable laser operated at 20 Hz, which can be tuned across the wavelength range 410 to 2100 nm, is used as the excitation source for all measurements. 520, 649, and 1500 nm light was used to populate the Er^{3+} $^4S_{3/2}$, $^4F_{9/2}$, and $^4I_{13/2}$ states, respectively. For 980 and 1500 nm-excited lifetime measurements, a 715 nm long pass filter is used to clean the laser spectrum prior to exciting the sample. A 750 nm short pass filter is used for excitation at 520 or 649 nm to block leaking light. In all cases, the excitation source is attenuated using a 1.0 optical density filter. All lifetime measurements are measured in the same quartz cuvettes as quantum yield measurements.

1.6 *In situ* diamond anvil cell spectroscopy

High pressure spectroscopy measurements are performed using a symmetric diamond anvil cell (DAC) with 500 µm diameter culets. The sample chamber consists of a 295 µm diameter hole in a pre-indented stainless steel gasket. This procedure closely follows those from our earlier publication.[5]

Loading the sample chamber. We dropcast colloidal UCNPs on a heated glass slide and scrape NPs from the resulting thin film. We load the nanoparticles into the sample chamber, which is then filled with silicone oil (density of 0.96 g/mL and viscosity of 0.5 Pa·s) to maintain a quasi-hydrostatic pressure environment. A small ruby ball (∼10 µm) is loaded near the sample as a pressure calibrant. The diamond anvil cell is closed and sealed with a loading pressure of ∼0.3 GPa.

Pressure calibration using ruby photoluminescence. Ruby photoluminescence (PL) is a well-characterized pressure calibrant. The PL spectrum has a doublet feature coming from the pressure-dependent crystal field splitting of Cr^{3+}.[6] For each pressure, we collect and average three ruby spectra under 488 nm illumination (Coherent Innova Argon-ion source), with a 500 nm blaze 1800 groove/mm grating (0.02 nm resolution), 10 µm slit, and 30 second acquisition time at 25 W/cm^2. The higher intensity emission peak is fitted to a Gaussian to determine its wavelength, λ, and compared to its value at ambient pressure, λ_o. We use the following equation to determine the pressure:[7,8]

$$P = (A/B)[(\lambda/\lambda_o)^B - 1] \tag{3}$$

where A = 1904 GPa and B = 7.715. Pressure values are rounded to the tenth decimal place, given uncertainty on the equation and resolution of the grating. Between each pressure point, we wait 5 to 15 minutes for the ruby PL to reach equilibrium.

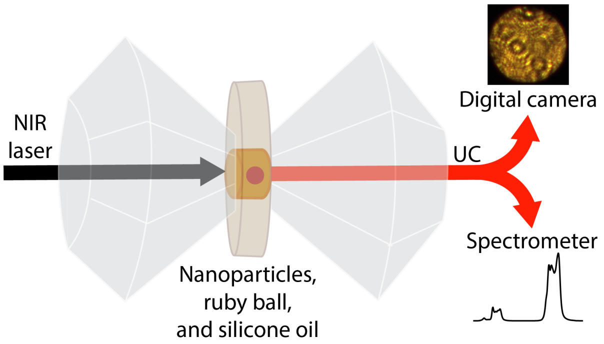

Figure S6: Experimental DAC schematic
A symmetric DAC is coupled to a 980 nm laser source. UCNPs, a ruby ball for pressure calibration, and silicone oil are loaded in the sample chamber between two diamond culets. UC emission is recorded by a digital camera and spectrometer.

Setup and upconversion measurement. The DAC is secured on a custom stage atop a Zeiss Axio Observer inverted microscope, ensuring that spectra are collected from the same sample area for each pressure point. Continuous wave (CW) 980 nm from a Coherent Ti:Sapphire laser source illuminates the DAC with an incident irradiance of ∼50 W/cm^2. We monitor the laser power using a pick-off right before the DAC. An 842 SP filter (Semrock BrightLine) is placed after the DAC to ensure that only the upconverted signal reaches the digital camera (Allied Vision Technologies) and spectrometer (Princeton Instruments ProEM eXcelon). A schematic is presented in Figure S6. Per pressure point, we collect three upconversion spectra using a 250 µm slit width and 500-Blaze 150 groove/mm grating (0.21 nm resolution). Similarly, we take optical images of the sample chamber with the digital camera, which reveals the corresponding color of upconversion emission.

Data processing. Reimman sums with widths of 0.21 nm are used to calculate the integrated intensity under the red and green emission peaks. We report the mean and standard deviation of the red to green ratio ($\frac{I_r}{I_g}$) from the three spectra collected at each pressure point. The percent change in $\frac{I_r}{I_g}$ from the ambient condition, $\frac{I_{r_o}}{I_{g_o}}$, is then calculated using the equation:

$$\Delta\frac{I_r}{I_g} = (\frac{I_r/I_g}{I_{r_o}/I_{g_o}} - 1) \cdot 100\% \tag{4}$$

We fit $\frac{I_r}{I_g}$ using a weighted linear least square fit in Matlab. Error is propagated through the division of the measured $\frac{I_{ro}}{I_{go}}$ and each fit is scaled so that the fitted $\frac{I_{ro}}{I_{go}}$ value is at 0%. The error on the slope or mechanosensitivity is taken as half of the 95% confidence interval.

2 Chemical composition

We quantify the lanthanide doping concentrations with inductively-coupled plasma optical emission spectroscopy (ICP-OES). 1-5mg of UCNPs are prepared assuming 50% of the measured mass is organics. With a target concentration of 10 mg/mL (nanoparticles in 3% aqueous nitric acid), we fully dissolve the UCNPs in ICP-grade nitric acid before adding the appropriate volume of water. ICP standards for each element are purchased from Ultra Scientific and used to create standard solutions based on expected compositions. We measure the absolute concentration (in ppm) of each element and convert them into molar percentages (Table S1). Note that the inert shell layer modifies the overall composition consistently across the core-shell nanoparticles, while the Y:Yb,Er-shelled retains a similar Yb:Er ratio as the cores. Some unexpected elemental content (e.g. 0.2% Lu in Gd-shelled NPs) are likely due to instrumental or sample preparation errors.

Table S1: Elemental analysis for core-shell nanoparticles

Sample (%)	Yb (%)	Er (%)	Y (%)	Gd (%)	Lu (%)
core	18.4	1.5	80.1	0.0	0.0
Y:Yb,Er-shelled	16.3	1.3	82.1	0.2	0.0
Y-shelled	4.8	0.4	94.8	0.1	0.0
Gd-shelled	5.6	0.4	24.9	68.9	0.2
Lu-shelled	5.4	0.4	24.3	0.0	69.9

3 Additional lifetime traces and discussion

3.1 Probing energy levels with direct and 980 nm excitation

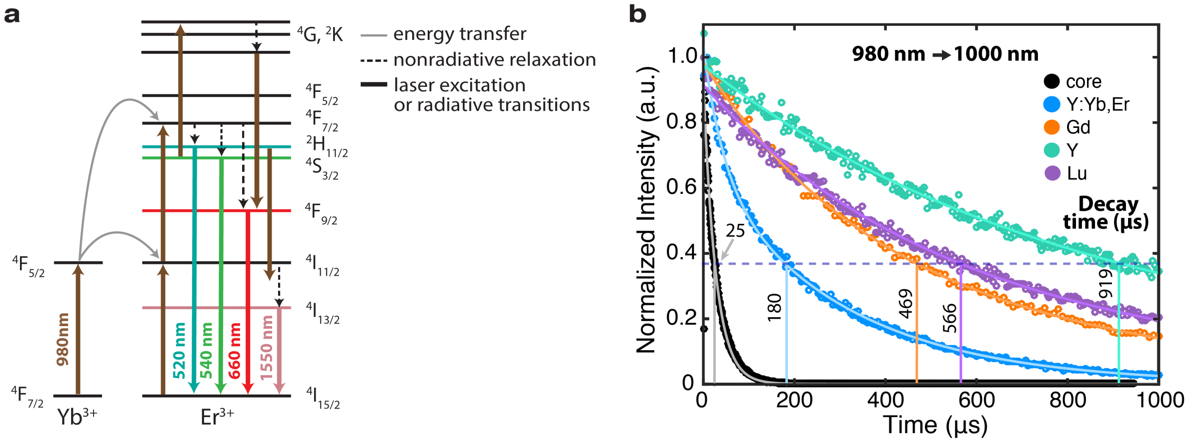

Figure S7: UC energy level diagram and lifetime traces for 980 nm → 1000 nm a) A simplified schematic of the multi-photon upconversion process, in which energy transfer between sensitizer Yb^{3+} ^{4}F$_{5/2}$ and emitter Er^{3+} ^{4}I$_{11/2}$ populates higher electronic states to yield emission in the visible (upconversion) or near infrared (downshifting). Prominent Er^{3+} radiative states include the green (^{4}H$_{11/2}$, ^{4}S$_{3/2}$), red (^{4}F$_{9/2}$), and near infrared (^{4}I$_{13/2}$). Note that the diagram follows from modeling and experimental literature on mostly hexagonal-phase UCNPs.[2,9] Additional experiments are required to fully map out the energetic pathways for cubic-phase UCNPs. b) Intensity decay curves (solid lines serve as a guide) for directly-excited Yb^{3+} ^{4}F$_{5/2}$ energy level. Decay times are defined as the time it takes unity intensity to reach 1/e (dashed line). Longer decay times for particles with an inert shell indicate better surface passivation and more time for energy migration and energy transfer to Er^{3+}. The enhancement of decay lifetimes for the inert Y shell is over 1.5x longer than the strained shells.

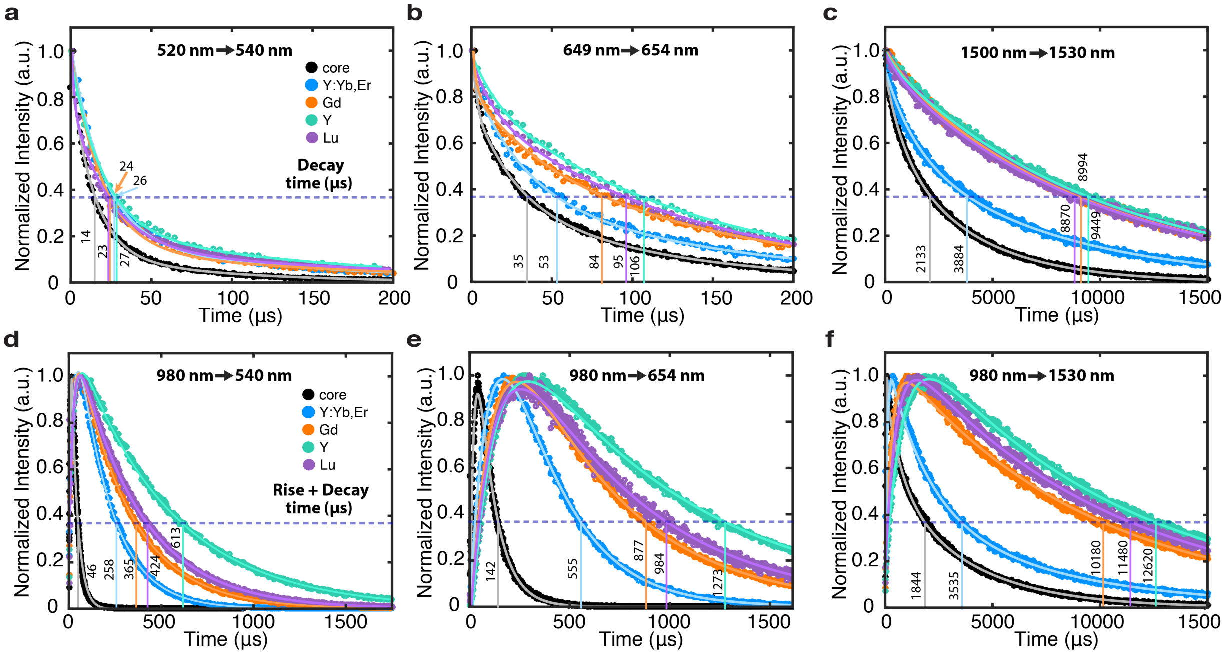

Figure S8: Lifetime traces under direct and 980 nm excitation
Direct excitation of the Er^{3+} a) green, b) red, and c) near infrared emission states. 980 nm excitation of the Er^{3+} d) green and e) red emission states, which are upconversion processes. f) Intensity decay curves for downshifted NIR emission. In almost every plot, decay lifetimes (summarized in Tables S2 and S3) increase in the following order: core, Y:Yb,Er-shelled, Gd-shelled, Lu-shelled, Y-shelled. Interestingly, Gd-shelled samples are more efficient than Lu-shelled samples in QY measurements (Figure 3). Opposing QY and lifetime trends suggest that radiative lifetimes are reduced with a compressive shell, supporting our hypothesis that the cores experience counteracting strain and local crystal field distortions.

3.2 Trends in the red to green ratio

Upconversion lifetime measurements can explain the trends in the red to green ratio $(\frac{I_r}{I_g})$ of Figure 3. Taking the ratio of the upconverted red enhancement to green enhancement in decay lifetime of Table S4, we get the values in Table S5. Both the unstrained samples have similar values of ∼0.6, while the strained samples have slightly higher values. Consistent with Figure 3, the strained samples are more "red" compared to the unstrained samples.

Table S2: Decay lifetimes under direct excitation

Emission	core (µs)	Y:Yb,Er-shelled (µs)	Y-shelled (µs)	Gd-shelled (µs)	Lu-shelled (µs)
540 nm	14	26	36	24	23
654 nm	35	53	106	84	95
1000 nm	25	180	919	469	566
1550 nm	2133	3884	9449	8994	8870

Table S3: Lifetime measurements under 980 nm excitation

Emission	Lifetime	core (µs)	Y:Yb,Er-shelled (µs)	Y-shelled (µs)	Gd-shelled (µs)	Lu-shelled (µs)
540 nm	rise	14	50	74	55	60
	decay	32	208	540	310	364
	total	46	258	613	365	424
654 nm	rise	41	167	290	234	255
	decay	101	388	983	643	729
	total	142	555	1273	877	984
1530 nm	rise	80	380	2061	1025	1472
	decay	1764	3155	10559	9155	10008
	total	1844	3535	12620	10180	11480

Table S4: Enhancement of decay lifetimes relative to the core

Excitation	Emission	core	Y:Yb,Er-shelled	Y-shelled	Gd-shelled	Lu-shelled
520 nm	540 nm	1	1.9	1.9	1.7	1.6
649 nm	654 nm	1	1.5	3.0	2.4	2.7
1500 nm	1530 nm	1	1.8	4.4	4.2	4.2
980 nm	540 nm	1	6.5	16.9	9.7	11.4
	654 nm	1	3.8	9.7	6.4	7.2
	1000 nm	1	7.2	36.6	18.7	22.5
	1530 nm	1	1.8	6.0	5.2	5.7

Table S5: Red enhancement to green enhancement

core	Y:Yb,Er-shelled	Y-shelled	Gd-shelled	Lu-shelled
1	0.59	0.58	0.66	0.63

4 Optical properties for various core sizes

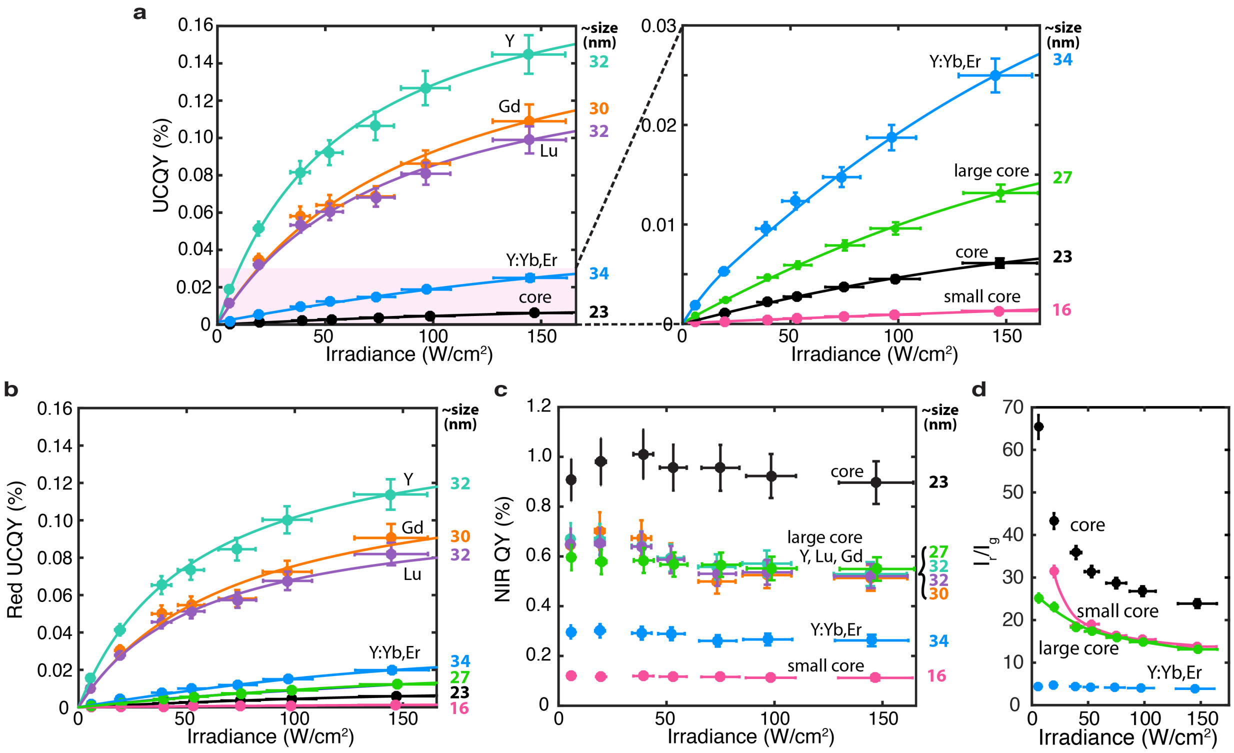

Figure S9: The size dependence of QY and red to green ratio
To determine the contribution of size on QY results, we synthesized both smaller and larger cores (Figure S1). Unsurprisingly, the QY enhancements are much smaller than those achieved by an inert passivation layer. a) Zoom-in plot showing the low efficiency of the cores over a range of irradiances. Generally, increasing size improves UCQY. Since red and NIR emission are especially desired for imaging in the biological window,[10] we also look at the trends for the b) red component of UCQY, typically above 80% of total UCQY values, as well as the c) downshifting process for the ratio of absorbed 980 nm photons that get emitted as 1550 nm photons (i.e. NIR QY). NIR QY is approximately constant over illumination power. Nanoparticles with an inert shell have similar NIR QY efficiencies of ∼0.5-0.6 %. For cores, NIR QY first increases with size and then decreases, because surface quenching both increases nonradiative losses and helps populate the Er^{3+} $^4I_{13/2}$ state. As described in previous work,[2] NIR QY relies on a competition of complex processes: surface quenching, multiphonon relaxation, Er-Er energy transfer, and spontaneous emission. d) Red to green ratio ($\frac{I_r}{I_g}$) for cores of various sizes. There are no clear trends based on size, but cores used in the main text have the highest $\frac{I_r}{I_g}$.

5 Detailed summary of DAC measurements

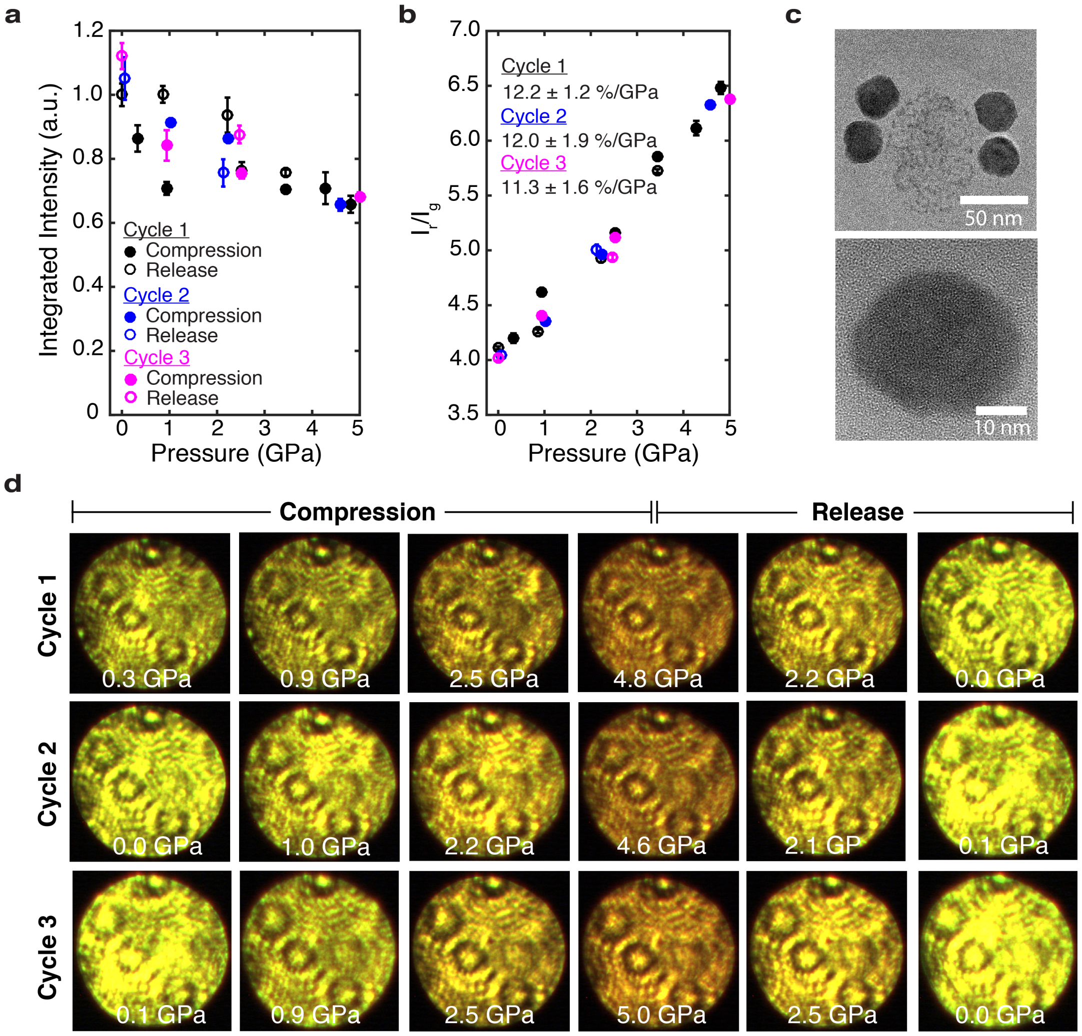

Figure S10: Mechano-optical response of Gd-shelled nanoparticles
For three complete pressure cycles, we track the integrated intensity and red to green ratio, $\frac{I_r}{I_g}$. a) Integrated intensity monotonically decreases with compression, but recovers upon release. b) $\frac{I_r}{I_g}$ increases linearly with compression. We define the slope as a measure for mechanosensitivity and list those values for Cycle 1 (black), Cycle 2 (blue), and Cycle 3 (pink). The Gd shell yields the largest color response. Additionally, mechanosensitivity is robust and stable over multiple pressure cycles. c) TEMs of post-DAC nanoparticles suggest that we induce minimal morphological or structural deformation even though pressures reach 5 GPa. d) Corresponding images of *in situ* upconversion emission support the positive linear trend of $\frac{I_r}{I_g}$. Color changes from yellow-green to orange are consistently observed. Note that the last release picture of each cycle or row is the first picture in the next cycle.

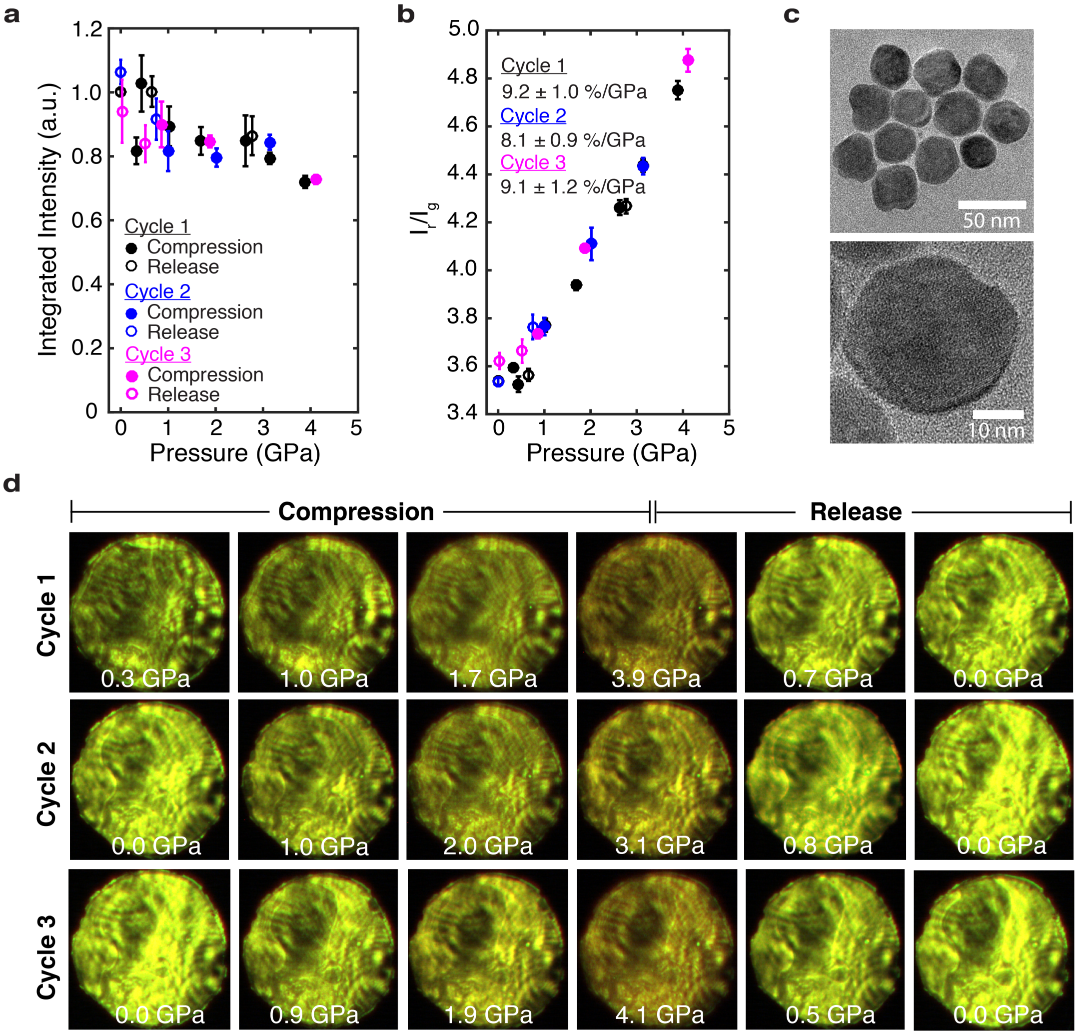

Figure S11: Mechano-optical response of Y-shelled nanoparticles
For three complete pressure cycles, we track the integrated intensity and red to green ratio, $\frac{I_r}{I_g}$. a) Integrated intensity monotonically decreases with compression, but recovers upon release. b) $\frac{I_r}{I_g}$ increases linearly with compression. We define the slope as a measure for mechanosensitivity and list those values for Cycle 1 (black), Cycle 2 (blue), and Cycle 3 (pink). Again, the mechanosensitivity is robust and stable over multiple pressure cycles. c) TEMs of post-DAC nanoparticles suggest that we induce minimal morphological or structural deformation even though pressures reach 5 GPa. d) Corresponding images of *in situ* upconversion emission support the positive linear trend of $\frac{I_r}{I_g}$. Color changes from green to yellow-brown are consistently observed. Note that the last release picture of each cycle or row is the first picture in the next cycle.

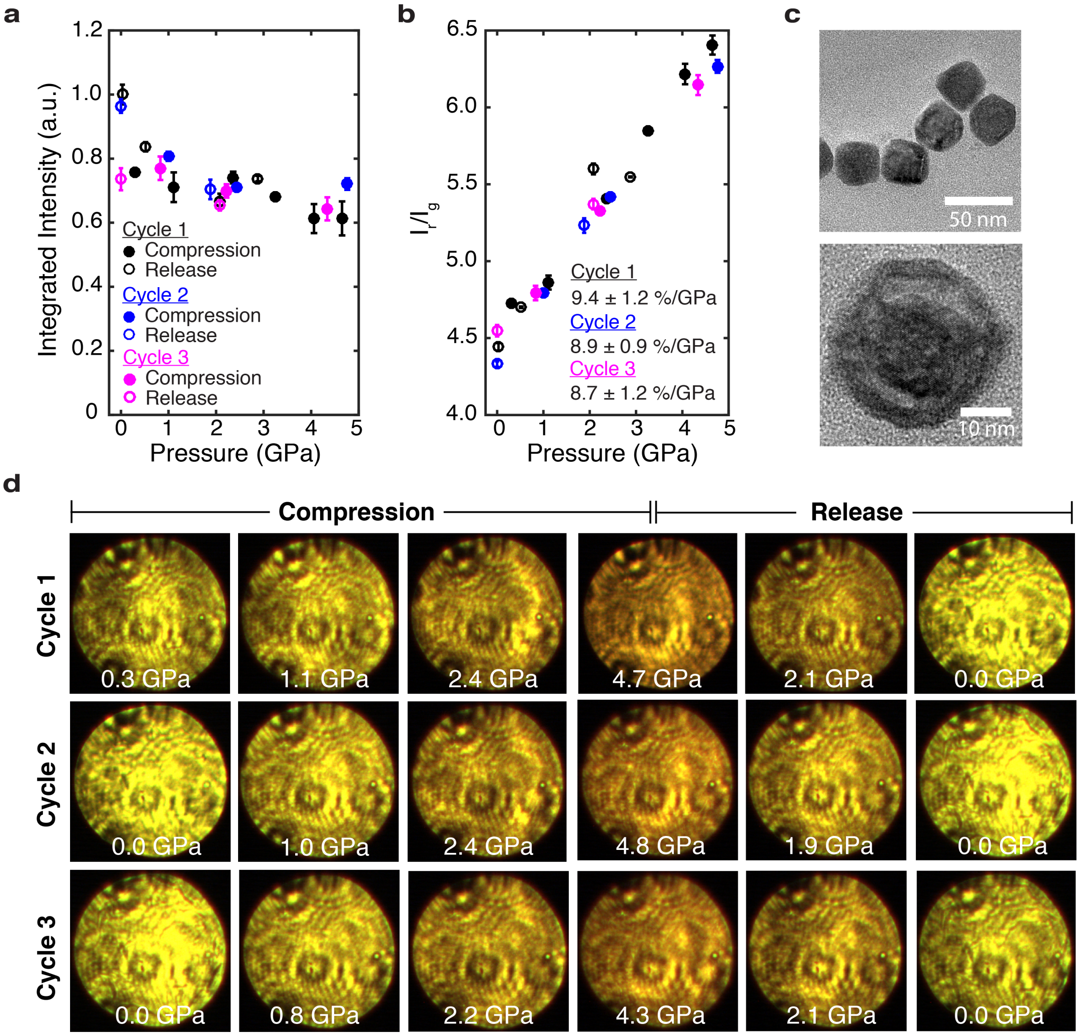

Figure S12: Mechano-optical response of Lu-shelled nanoparticles
For three complete pressure cycles, we track the integrated intensity and red to green ratio, $\frac{I_r}{I_g}$. a) Integrated intensity monotonically decreases with compression, but recovers upon release. b) $\frac{I_r}{I_g}$ increases linearly with compression. We define the slope as a measure for mechanosensitivity and list those values for Cycle 1 (black), Cycle 2 (blue), and Cycle 3 (pink). Again, the mechanosensitivity is robust and stable over multiple pressure cycles. c) TEMs of post-DAC nanoparticles reveal electron beam damage. This is consistent with prior findings that cores disintegrate more easily with tensile shells.[11] d) Corresponding images of *in situ* upconversion emission support the positive linear trend of $\frac{I_r}{I_g}$. Color changes from yellow to orange are consistently observed. Note that the last release picture of each cycle or row is the first picture in the next cycle.

6 Synthesizing nanoparticles with thicker Gd shells

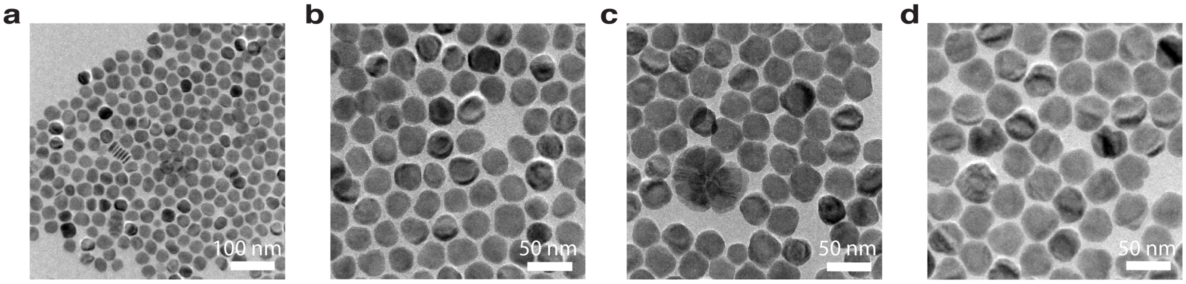

Figure S13: Challenges of heteroepitaxial growth with a compressive shell
a) and b) are TEMs of the inert Gd sample used in the main text at different magnifications. We note that there are some rod-like nanoparticles present, which should not have a significant effect on the structural, optical, and force-sensitivity measurements due to their relatively low concentration. Additionally, we attempted to increase the inert Gd shell thickness for better size comparisons, but encountered synthetic challenges. Namely, island-like growth in the form of large flower-like nanoparticles can be seen in c), as well as anisotropic morphology in d). These experiments suggest that a critical thickness for strain relaxation exists, much like it does for thin film epitaxial growth.

References

(1) Li, X.; Liu, X.; Chevrier, D. M.; Qin, X.; Xie, X.; Song, S.; Zhang, H.; Zhang, P.; Liu, X. *Angew. Chem.* **2015**, *127*, 13510–13515.

(2) Fischer, S.; Bronstein, N. D.; Swabeck, J. K.; Chan, E. M.; Alivisatos, A. P. *Nano Lett.* **2016**, *16*, 7241–7247.

(3) Pawley, G. *J. Appl. Crystallogr.* **1981**, *14*, 357–361.

(4) Wisser, M. D.; Fischer, S.; Maurer, P. C.; Bronstein, N. D.; Chu, S.; Alivisatos, A. P.; Salleo, A.; Dionne, J. A. *ACS Photonics* **2016**, *3*, 1523–1530.

(5) Lay, A.; Wang, D. S.; Wisser, M. D.; Mehlenbacher, R. D.; Lin, Y.; Goodman, M. B.; Mao, W. L.; Dionne, J. A. *Nano Lett.* **2017**, *17*, 4172–4177.

(6) Yamaoka, H.; Zekko, Y.; Jarrige, I.; Lin, J.-F.; Hiraoka, N.; Ishii, H.; Tsuei, K.-D.; Mizuki, J. *J. Appl. Phys.* **2012**, *112*, 124503.

(7) Mao, H.; Mao, W. L. *Treatise Geophys.* **2007**, *2*, 231–267.

(8) Mao, H.; Xu, J.-A.; Bell, P. *J. Geophys. Res.: Solid Earth* **1986**, *91*, 4673–4676.

(9) Berry, M. T.; May, P. S. *J. Phys. Chem. A* **2015**, *119*, 9805–9811.

(10) Hemmer, E.; Benayas, A.; Légaré, F.; Vetrone, F. *Nanoscale Horiz.* **2016**, *1*, 168–184.

(11) Johnson, N. J.; van Veggel, F. C. *ACS Nano* **2014**, *8*, 10517–10527.